

Taming Flat Bands with Breathing Superlattices

Moru Song^{1,4}, Jinyu Hu², Lina Shi^{2*}, Yongliang Zhang^{1*},
Kai Chang^{3*}

¹State Key Laboratory of Semiconductor Physics and Chip Technologies,
Institute of Semiconductors, Chinese Academy of Sciences, Beijing
100083, China.

²State Key Laboratory of Fabrication Technologies for Integrated
Circuits, Institute of Microelectronics, Chinese Academy of Sciences,
Beijing 100029, China.

³Center for Quantum Matter, Zhejiang University, Hangzhou 310027,
China.

⁴College of Materials Science and Opto-electronic Technology, University
of Chinese Academy of Sciences, Beijing 100049, China.

*Corresponding author(s). E-mail(s): shilina@ime.ac.cn;
ylzhanglight@semi.ac.cn; kchang@zju.edu.cn;

Abstract

Flat bands have become a pillar of modern condensed matter physics and photonics owing to the vanishing group velocity and diverging density of states. Here, we present a paradigmatic scheme to construct arbitrary flat bands on demand by introducing a new type breathing superlattice, where both the number and spectral positions of isolated flat bands can be continuously tailored by simply controlling the breathing strength. Microscopically, the momentum-independent interband scatterings near the band edge protect them robust against weak intra-cell disorder. By dimensional reduction, we establish a duality between the one-dimensional (1D) breathing superlattice and the 2D Harper-Hofstadter model, where cascade flat bands naturally emerge as the different orders of Landau levels in the weak magnetic flux limit. As a proof of concept, photonic flat bands at optical frequencies are experimentally demonstrated with all-dielectric photonic crystal slabs. Finally, we generalize our scheme to 2D systems to realize partial and omnidirectional flat bands, and discuss the achievement of high-quality factors. Our findings shed new light on the manipulation of flat bands with high band flatness and large usable bandwidth, paving the way for the development of advanced optical devices.

Keywords: Flat bands, photonic crystal, Landau levels, duality

Introduction

Band dispersion, essential for understanding the wave dynamics in periodic systems, can be tailored with artificial lattices containing carefully designed building blocks [1–5]. In optics and photonics, engineering the band dispersion is central to mold light propagation [6] and tailor light-matter interactions [3, 7, 8], leading to a variety of novel devices such as microstructured fibers [9, 10], metalenses [11] and analog optical computing [12, 13]. Recently, flat bands have attracted significant attention in photonic systems owing to their unique ability to trap light [14–18]. The narrow bandwidth of flat bands leads to slow light with vanishing group velocity and diverging photonic density of states (DOS) [19], thereby enhancing light-matter interactions for practical applications including lasers [20], sensors [21], filters [22], and compact free-electron light sources [23].

Generally, the localization nature of flat bands is associated with the compact localized states (CLSs), where the wave functions are confined to specific regions in real space due to destructive interference. In analogy to electronic systems, several systematic methods have been proposed to generate flat bands in photonic systems. The standard construction of flat bands utilized line graphs and bipartite lattices with geometric frustration, such as Kagome [24–29], Lieb [28–32] and dice lattices [33], where the CLSs are formed on specific sublattices and the number of flat bands is determined by the unequal number of orbitals in different sublattices [34]. Another widely recognized mechanism involves quasi-periodic [35] or fractal lattices [36]. Very recently, there has been emerging interest in exploiting flat bands in moiré [37–39] and strained engineering superlattices [40–45], along with their photonic analogs [46–54], by folding and flattening bands through pseudo-magnetic fields. Despite these intensive parallel efforts, however, how to construct arbitrary flat bands on demand remains elusive. For instance, flat bands in line-graphic and bipartite lattices necessitate specific symmetry under nearest-neighbor hopping, which are too restrictive for optical systems [34]. Furthermore, isolating flat bands from dispersive bands requires modified hopping parameters to remove symmetry-protected band touching points [55, 56]. To establish destructive interference, non-crystalline systems need specific forms of hoppings at large scale, which hinder the implementation and engineering of flat bands. Moreover, moiré superlattices require precise alignment at the magic angles to create macroscopic moiré patterns [37, 48, 54]. Most importantly, all known systems possess a fixed number of flat bands, and there has not been a systematic strategy to engineer isolated flat bands with tunable numbers and extreme small bandwidth in a simple platform.

In this work, we present a general scheme to construct isolated super flat bands on demand by introducing breathing superlattices. Compared to previous studies, we show that both the number and spectral positions of flat bands can be continuously engineered by simply controlling the breathing strength of sublattices. In particular,

pairs of isolated flat bands can be cascadingly peeled out from the folded dispersive bands. Analysis based on the continuum model (CM) and the rigorous Maxwell eigenvalue problem demonstrate that these flat bands arise from a novel mechanism due to the momentum independent interband scatterings among folded bands near the band edge, which also protect them robust against weak intracell disorder. To be specific, we show that the 1D CM Hamiltonian is dual to the 2D Harper-Hofstadter (HH) model [57] with an enriched higher dimensional topology beyond the effective mass approximation. Unlike previous studies where flat bands typically mimic the lowest Landau levels (LLs) induced by pseudo-magnetic potentials (e.g., moiré potentials) through quantum geometric properties of wave functions [38, 42], here the cascade flat bands precisely correspond to higher-order LLs arising from constant dual magnetic flux via dimensional reduction [58]. The non-trivial topology leads to topological edge states resided in the minigaps. As a concrete example, the formation and evolution of flat bands at optical frequencies are experimentally demonstrated with all dielectric photonic crystal slabs. Finally, we apply the methodology to 2D systems for the design of partial and omnidirectional flat bands which may reveal 4D topologies, and discuss the realization of flat bands resonances with wide-angle ultra-high quality factors (Q-factors).

Results

Analytical models

For simplicity, let us illustrate the scheme by introducing the breathing superlattice in 1D. We start by considering an enlarged unit cell containing N sites in a simple 1D periodic lattice with lattice constant a_0 . To construct the breathing superlattice, we divide the enlarged unit cell into two equal sublattices, and perturb them either positively (expanded) or negatively (shrunk) without altering the size of the larger unit cell (See Fig. 1). Consequently, each sublattice comprising a simple chain of $N/2$ sites with different spacings $a_{1,2} = a_0(1 \pm \delta)$, where the shifting parameter δ characterizes the breathing strength. The real-space tight-binding (TB) Hamiltonian takes the form

$$\hat{H} = \mu \sum_{Ii} \hat{c}_{Ii}^\dagger \hat{c}_{Ii} + t \sum_{R_{Ii} \neq R_{Jj}} e^{-\xi |R_{Ii} - R_{Jj}|} \hat{c}_{Ii}^\dagger \hat{c}_{Jj}, \quad (1)$$

where \hat{c}_{Ii}^\dagger and \hat{c}_{Ii} are creation and annihilation operators at site i of the I th unit cell, μ is the on-site energy, and $t e^{-\xi |R_{Ii} - R_{Jj}|}$ denotes the hopping between sites R_{Ii} and R_{Jj} with ξ controlling the coupling strength. For weakly shifted sublattices, the nearest-neighbor hoppings are approximate to $t e^{-\xi a_0(1 \pm \delta)} \approx t_0(1 \mp \delta_T)$, where $t_0 = t e^{-\xi a_0}$ and $\delta_T = \xi a_0 \delta$. Note that, under this approximation, the structure reduces to the Su-Schrieffer-Heeger (SSH) model [59] with $N = 2$. When $\delta = 0$, the superlattice reduces to a simple chain that trivially supports a dispersive band $E_k = t_0 \cos(ka_0)$. When $\delta \neq 0$, the superlattice folds the original band structure into N subbands, flattening them into flat bands by varying shift parameters. As shown in Figs. 2(a), the TB-based

band structure for the breathing superlattice of $N = 14$ shows two well-separated flat bands below the dispersive band.

To gain a deep insight for the flat bands, we project the TB Hamiltonian onto the truncated plane wave basis [60], and obtain the following effective CM Hamiltonian near the Γ valley (see Supplementary S1 for deviation of CM):

$$\hat{H}(q) = \sum_n \left[\frac{(q + Q_n)^2}{2m^*} + \mu \right] \hat{b}_n^\dagger \hat{b}_n + \sum_s w_s \hat{b}_n^\dagger \hat{b}_{n+s}, \quad (2)$$

where $m^* = t_0/a_0^2$ is the effective mass at Γ , q is the wave vector, $Q_n = nq_0$ with $q_0 = 2\pi/Na_0$ is the n th reciprocal lattice site, $\hat{b}_n^\dagger(q) = \sum_{Ii} e^{i(q+Q_n)R_{Ii}} \hat{c}_{Ii}^\dagger$. The first term in Eq. (2) determinates the dispersion of the n th folded subband, w_s ($s = 1, 2, \dots$) denotes the interband scattering between the n th and $(n+s)$ th subbands. At large N , the scattering strength w_s becomes independent from the momentum. At certain values of δ , w_s dominates $(q + Q_n)^2/2m^*$ terms when $n < M$, resulting in M flat bands (See Microscopic mechanism for detailed explanation). The CM band structures presented in Fig. 2(a) show excellent agreement with TB, confirming the existence of flat bands in breathing superlattices. In real space, the interband scattering process leads to destructive interference of light in one of the sublattices, demonstrating the localization nature of flat bands modes. The viewpoint of CM clarifies the origin of flat bands from the momentum-independent interband scatterings, especially in large N . Notice that Eq. (2) is a 1D version of the Bistritzer-MacDonald model describing twisted transition metal dichalcogenides (tTMDs) at Γ [37, 39]. Similar results can be obtained by projecting the Maxwell equation into the plane wave basis directly (see Method at section Effective model). As we will show below, flat bands physics can be enriched by higher dimensional topology when go beyond this effective mass CM model.

Photonic flat bands

We now consider all-dielectric PhCSs consisting of 1D lattice of meta-gratings as the photonic realization of the proposed model at $N = 14$. To realize breathing hoppings, the strip widths in different sub-lattices are assumed to be $d_1 = \kappa a_1$ and $d_2 = \kappa a_2$. Fig. 2(a) presents the band structures for the TM polarization, which are numerically calculated by the guided mode expansion (GME) method [61]. Here, the structural parameters are $a_0 = 190$ nm, $\kappa = 0.6$, $h = 144$ nm, $\delta = 0.06$. The permittivity of the dielectric material is $\varepsilon_m = 7.022$ (TiO₂). As shown in the figure, two flat bands are observed with bandwidths of 0.2 and 2 nm, which agree with TB and CM. The electric fields at Γ shown in Fig. 2(c, d) are strongly confined to the shrunken region, with no node (lower band) and one node (higher band). Similar field distributions are observed for other k points (see Supplementary Fig. S8), suggesting similar features as LLs for the 2D electron gas in an external magnetic field.

It is instructive to investigate the evolution of the band structure with respect to the breathing strength. Fig. 3 shows the calculated photonic band structures for PhCs with $N = 14$ and δ varying from 0 to 0.13. For $\delta = 0$, there are two folded dispersive

bands separated by a large band gap, which are similar to the conduction- and valence-like electronic bands in semiconductors. Away from $\delta = 0$, a band gap opens at K in both conduction and valence bands, resulting in a pair of isolated bands. As shown in Fig. 3(b), the gap width increases further with δ . After the gap opening at K , the first band crossing point at Γ opens and generates a second pair of flat bands. Further TB calculation shows the rate of gap opening at K is linear with δ , which is faster than the rate $\propto \delta^2$ at Γ (see Supplementary S6 for details). Consequently, the second pair bands become flat at $\delta = 0.12$ [Fig. 3(c)].

Upon further increase δ , two new pairs of flat bands emerge, while the other flat bands move into the gap center [Figs. 3(c,d)]. Consequently, the first pair of flat bands become dispersive for $\delta = 0.1$ [Fig. 3(e)], and form a Dirac cone when the gap at Γ closes at $\delta = 0.11$ [Fig. 3(f)]. When δ increases further, the Dirac cone at Γ re-opens, leading to another Dirac cone at K , as shown in Figs. 3(g) and 3(h). When δ varies continuously, Dirac cones at the higher symmetry points form and split repeatedly, along with the emergence of new pairs of flat bands. As a result, both the number and spectral positions of flat bands can be engineered by simply shifting the sublattices. Figs. 3(i) and 3(j) depict the evolution of the bandwidth of the first four pairs of flat bands, which exhibits a similarly non-monotonous dependence on δ where each band has a minimum bandwidth at a specific $\delta = \delta_M$. Additionally, bands near the forbidden zone are narrower than remote ones for small δ , while wider for large δ because of the mutual interplay between flattening and re-dispersion. It should be mentioned that the number of flat bands is limited by the band gap's width of the original structure, which should be carefully designed in practice.

Microscopic mechanism

Physically, CM can be viewed as TB in the reciprocal lattice as illustrate in Fig. 4(a). To gain quantitative insights into the underlying physics of flat bands, we simplify the CM Hamiltonian by only considering the scattering between nearest-neighbor subbands with $s = 1$. Then, Eq. (2) can be recast into the iterated matrix form:

$$H_m(q) = \begin{bmatrix} (q - mq_0)^2 & \gamma I_{m-1} & 0 \\ \gamma I_{m-1}^T & H_{m-1}(q) & \gamma I_{m-1}^T \\ 0 & \gamma I_{m-1} & (q + mq_0)^2 \end{bmatrix}, \quad (3)$$

where $H_0 = q^2$, $I_m = [1, 0, \dots, 0]$ and $\gamma = 2m^*w_1$ is the reduced interband scattering. The cascadingly generated flat bands can be interpreted by Eq. (3). To be specific, we note that the iterated order m naturally defines two sequenced energy windows, i.e., the diagonal elements $E_q^{(0)}(m) = (q \pm mq_0)^2$. For a fixed m , the off-diagonal elements of $H_m(q)$ become comparable to $E_q^{(0)}(m)$ as γ increases, suggesting a band gap opens at Γ when γ approaches $E_\Gamma^{(0)} \propto m^2$, and at K when γ near $E_K^{(0)} \propto (\pm m + 1/2)^2$. Consequently, flat bands emerge consecutively by continuously increasing m and γ . Specifically, the subband arising from $E_q^{(0)}(0)$ can be fitted with a polynomial form

from Eq. (3) (see Supplementary S8 for details),

$$E_1(q, \gamma) = F_0 + F_2 q^2 + F_4 q^4. \quad (4)$$

Here we set unit $q_0 = 1$, $F_0 = \sum_{n=0}^2 c_n^{(0)} \gamma^n$ and

$$F_m = \left(1 + c_3^{(m)} \gamma^3 / \left(c_0^{(m)} + c_1^{(m)} \gamma + c_2^{(m)} \gamma^2 \right) \right)^{-1},$$

for $\gamma > 1/4$; $F_2 = 1 - 6\gamma^2$ and $F_4 = 0$ for $\gamma < 1/4$, where $c_n^{(m)}$ are fitting parameters. The fitted bands for different γ ranging from 0 to 1.5 presented in Fig. 4(c) are consistent with the numerical diagonalization of Eq. (3). Importantly, $c_n^{(m)}$ vary slowly with γ , and take constant values within a certain range of γ , leading to weak dispersion at large γ (see Supplementary Tab. S1). If the scattering strength γ is fixed, the effect of the site number N is captured by the scaling parameter $q_0 \propto N^{-1}$. As shown in Fig. 4(f), the number of flat bands increases with N . This relationship is further verified through the GME calculations as depicted in Fig. 4(g). Notably, we can renormalize γ with N by $\gamma' = \gamma/q_0^2$ in the large N limit (see Supplementary S9 for derivations), which suggests that the effects of γ and N are qualitatively equivalent in the CM framework.

The interband scattering mechanism can be further confirmed by an exact optical model. To this end, we consider the rigorous Maxwell eigenvalue problem: $\hat{\Theta} \mathbf{H} = (\omega/c)^2 \mathbf{H}$, where $\hat{\Theta} = \nabla \times (\epsilon^{-1}(\mathbf{r}) \nabla \times)$ [6]. In the plane wave basis, $\hat{\Theta}$ of the 1D breathing superlattice is given by (see Supplementary S4 A for derivations of $\hat{\Theta}$ operator).

$$\hat{\Theta} = \sum_{ij} h_q(g_i, g_j) \tilde{\epsilon}(g_i - g_j) \hat{b}_i^\dagger \hat{b}_j, \quad (5)$$

where $g_i = 2i\pi/Na_0$ labels the reciprocal lattice site, and $h_q(g_i, g_j) = q^2 + q(g_i + g_j) + g_i g_j$ describes the dispersion relation of subbands ($i = j$) and interband scattering ($i \neq j$). The Fourier component of the inverse permittivity reads,

$$\tilde{\epsilon}(g) = \epsilon_m^{-1} \delta_{g,0} + \frac{i(1 - \epsilon_m^{-1})}{g} \Sigma(g), \quad (6)$$

where $\Sigma(g) = \sum_{n=0}^{N-1} (e^{i\kappa g a_n} - 1) e^{-igR_n}$ and $a_n = R_{n+1} - R_n$. The structural information is encoded in the interband scattering via the sum $\Sigma(g)$. For the case $\delta = 0$, the formation of the band gap comes from the scatterings between the i th and $(i + tN)$ th bands with $t \in \mathbb{Z}$ corresponding to the interference condition (IFC) $\sum_n e^{igtR_n} = \sum_n e^{i2\pi nl/N} = \delta_{l,tN}$. For $\delta \neq 0$, there are additional scatterings between the i th and $i \pm (tN \pm j)$ th bands ($j = 1, 2, 3, \dots$), which leads to the formation and evolution of flat bands. When $\delta = 0.07$, IFC breaks slightly and interband scatterings appear at $j = 1, 2$, leading to two flat bands. However, for larger $\delta = 0.23$, the strongly broken IFC leads to multi-band scatterings involving very large j , resulting in the redispersion of flat bands. Interestingly, it is sufficient to only consider $i \pm (N \pm 1)$ th bands scattering to generate flat bands, as shown in the minimal effective model in Fig.

4(e) (see Supplementary Fig. S6 and section Effective model in Method for details). Moreover, from the expression of $h_q(g_i, g_j)$, the dispersion effect is negligible in the scatterings between the i th and $i \pm (N \pm 1)$ th bands when $g \gg q$, which validates assumption of the momentum-independent interband scattering at large N . Meanwhile, the additional scatterings near the band edge, i.e. $1 \leq j \ll N$, enable these flat bands robust to weak intra-cell disorder (Fig. 5(f)), where the frequency and bandwidth of flat bands change slightly when the disorder strength smaller than $a_0/8$ (see Supplementary S7 for details).

Dual LLs and topological origin

After establishing the microscopic origin of flat bands from the momentum-independent interband scatterings, we now exploit the global topology of the breathing superlattices. As demonstrated in Fig. 2(c,d), the eigen-fields of the flat bands exhibit similar nodal structures as the field patterns of different orders of LLs for the 2D quantum dynamics of charged particles in an external magnetic field, which indicates a topological origin for these flat bands. However, our system is a 1D periodic lattice without introducing time reversal or inversion symmetry breaking terms, which differs from conventional Chern or valley Chern insulators. To motivate, we reconsider the CM by considering the intraband dispersion beyond the effective mass approximation,

$$H = \sum_{n,q} t_0 \cos((q + nq_0)a_0) b_{n,q}^\dagger b_{n,q} + w_1 \sum_{s=\pm 1} \hat{b}_{n,q}^\dagger \hat{b}_{n+s,q} \quad (7)$$

where $q \in [0, q_0)$. Eq. (7) supports an unexpected duality between our 1D system with the HH model [57] on the reciprocal lattice. To this aim, we adiabatically move the sites inside unit cell. In periodic boundary condition (PBC), this process brings no physical consequence except that an auxiliary pure gauge k_ϕ is introduced to the momentum. By substituting $qa_0 \rightarrow k_m = qa_0 + k_\phi \in [0, 2\pi)$, a fictitious dimension can be defined by performing Fourier transform of $b_{n,k_m}^\dagger = \frac{1}{\sqrt{N_m}} \sum_m e^{ik_m m} b_{m,n}^\dagger$, which yields the following lattice Hamiltonian (see Supplementary S2 for derivations):

$$H = \sum_{m,n} \frac{t_0}{2} e^{in\Phi} b_{m+1,n}^\dagger b_{m,n} + w_1 b_{m,n+1}^\dagger b_{m,n} + h.c., \quad (8)$$

where $\Phi = q_0 a_0 := \Phi_0/N$ with $\Phi_0 = 2\pi$, m and n label the reciprocal lattice points associated with the fictitious and physical dimensions, respectively. Eq. (8) is formally equivalent to the Hamiltonian of the 2D HH model, where Φ takes the role of the magnetic flux. In the HH model $\Phi/\Phi_0 = P/Q$, where Φ_0 is the flux quantum and P, Q are integers [57, 62]. In our 1D superlattice, we take $P = 1$ with $Q = N$ representing site number per unit cell. One of the central features of the HH model is the Hofstadter's butterfly, which is the self-similar fractal spectral response with increasing the external magnetic field. The calculated dependence of the energy spectra on q_0 for $P = 1$ sector clearly shows a typical Hofstadter butterfly pattern, which confirms the dual picture. In the HH model, the Hofstadter butterfly pattern reduces to LLs in the weak field limit. In our system, this picture explains the cascade LLs at large N , as shown

in Fig. 4(h). Additionally, the LL picture fails at strong field, which corresponds to the absence of flat bands at small N .

Besides the formal equivalence, the topological origin of our system is connected with the HH model through dimensional reduction [63]. Physically, the HH model describes the lattice model of the quantum Hall effect [62], where each energy band has a nontrivial Chern number. In our system, the Chern number can be interpreted as the integer charge, i.e. the field strength per unit cell, pumped over a cycle of k_ϕ from 0 to 2π . During the pump process, the inversion symmetry is presented only at $k_\phi = 0$ and $k_\phi = \pi$, where the inversion center locates at the center of the shrunken or expanded region (corresponding to $\delta > 0$ or $\delta < 0$, respectively). By the dimensional reduction process described above, the charge polarization varies between these two cases, and the difference defines a \mathbb{Z}_2 Zak phase ϕ_{Zak} , which is protected by inversion symmetry [63]. The physical meaning of ϕ_{Zak} corresponds to the Wannier center position of a given band (see Method, Numerical simulation and Supplementary S3). Fig. 4(e) shows one loop winding of the Wannier center along the unit cell as k_ϕ varies. The spectral flow for the cycle is obtained for $N = 40$ with open boundary calculation (OBC) in Fig. 4(i), with the corresponding band structure shown in Fig. 4(h). To be specific, ϕ_{Zak} becomes nontrivial when two 1D edge states cross at $k_\phi = \pi$, leading to conner states in the minigap. Additionally, flat bands originating from the same conduction (or valence) bands have the same ϕ_{Zak} , exhibiting the same node structures as LL wave functions (see Supplementary Figs. S2 and S3).

Numerical calculation for $N = 40$ on a 400×50 grid in the 2D (k, k_ϕ) space yields $C = 1$ for both the initially emerged flat band (lowest LL) and the subsequent flat bands (higher LLs). This result is consistent with the Wannier centers winding shown in Fig. 4(e) for different flat bands, confirming our dual picture. As a result, fractional charges are observed at the boundaries, where the number of nodes increases with their order, as shown in Fig. 4(j). Also note that introducing k_ϕ to achieve duality with LLs is feasible only in 1D systems, where the CM possesses a finite energy upper bound (such as the cosine term in Eq. (7)). Although it is possible, directly extending this method to 2D superlattices becomes more complicated because there lacks a straightforward analogy to LLs, and the traditional usage of CM such as Dirac [48] or parabolic-like term [39] is no longer valid.

Experimental demonstration

For the experimental realization of photonic flat bands, a large band gap is crucial to suppress the undesired interband scatterings. For a fixed photonic structure, especially 1D system, multiple band gaps at different wavelengths. Typically, the band gap in the long wavelength is crucial for achieving flat bands with high Q-factors. See, for example, flat bands shown Fig. 5 (k, l). However, flat bands in higher gap are often easier to observe due to the stronger coupling with free space modes and the compatibility with the effect of substrate.

Here, we fabricate all-dielectric PhCSs on TiO_2 membranes by using standard nanofabrication technology combining electron-beam lithography and dry etching process. Representative scanning electron microscope (SEM) images of the sample are shown in Fig. 5 (a-c), where a 144 nm thick TiO_2 and an intermediate ITO layer are

deposited on the SiO_2 substrate by using atomic layer deposition. The filling factor of the sample is 0.6. In Fig. 5, the measured TM-polarized band structure in higher gap shows two flat bands, which are consistent with numerical calculations in a broad frequency range. In addition, as shown in Fig. 5 (h-j), flat bands appear cascadingly and shift towards shorter wavelength. Because the Q-factors decrease rapidly with δ , the measured bands are blurred except the uppermost flat band, which remain distinct due to the weak leakage.

Discussion

2D generalizations

The proposed 1D breathing superlattices can be readily extended to higher dimensions. Fig. 6(a) presents the simplest generalization to 2D, where the breathing superlattice is along the x -axis and remains a simple periodic lattice along the y -axis. The corresponding photonic band structure for a PhCS consisting of 2D hole arrays of the proposed partial breathing superlattice milled in the free-standing TiO_2 membrane is shown in Fig. 6 (c), where partial flat bands are observed along the Γ - X direction. Similar to 1D systems, the distribution of the magnetic field shows that light is strongly localized in the shrunken region. Obviously, it is easy to realize partial flat bands in an arbitrary direction by choosing the orientation of the breathing superlattice.

To achieve omnidirectional flat bands requires structural breathing in both directions. A representative 2D breathing superlattice created from a simple triangular lattice is shown in Fig. 6 (b), where the expanding and compressed regions are respectively shaded with green and purple (see Method, Construction of 2D breathing lattice). Fig. 6 (d) presents the calculated band structures of a free-standing PhCS consisting of hole arrays milled in the membrane. It is shown that there exist two flat bands at higher frequencies spanned over the full Brillouin zone, and four weakly dispersive bands near $5.1c/a$. Interestingly, these flat bands are reminiscent of those generated from Γ valley tTMDs [39]. Moreover, flat bands in 2D breathing superlattices emerges cascadingly when δ increases, which is similar to 1D cases (see Supplementary Fig. S11). As shown in the inset of Fig. 6 (d), however, these omnidirectional flat bands appear in groups due to the protection of an approximated C_6 symmetries, which indicates that the lattice symmetry offers an additional degree of freedom in designing flat bands in 2D.

High quality flat bands

The Q-factor of optical resonances is essential for increasing the life time of quasi-particles in light-matter interactions. Meanwhile, the enhanced light-matter interactions in general flat bands systems are usually attributed to CLSs [47, 64, 65]. It is interesting to simultaneously achieve both of them in the breathing superlattices with specific design of parameters (see Method Numerical simulations). As shown in Fig. 5 (k, l), the transmission spectra of a free standing PhCSs is calculated through the rigorous coupled wave approximation (RCWA) method at $N = 14$. Without geometry

optimization, the Q-factor of flat bands can reach $Q = 1.5 \times 10^5$, which is comparable to the finely tuned high quality flat bands in moiré lattice [64]. The calculated high Q-factor has a similar mechanism as the quasi-bound states from band folding [66]: when $\delta = 0$, the dispersive bands are exact bound states below the light cone; While for $\delta \neq 0$, the structural breathing folds the dispersive bands above the light cone, and the inter-band scatterings introduce weak leakage into the free space, generating high-Q flat band resonances. Remarkably, different from high Q-factor modes only appear at specific k-points in usual cases [64, 67], the high Q-factor flat band resonances in Fig. 5(k, l) exist within a wide range of incident angles, making them an ideal platform for applications such as phase synchronization of nanolaser arrays [68], Kerr nonlinearity [69], and wide view optoelectronic devices [70].

In summary, we have demonstrated a general strategy to construct cascade flat bands on demand with breathing superlattices, which have a topological origin. By simply varying the breathing strength, both the number and spectral positions of flat bands can be continuously engineered, which holds great potential for the development of advanced wide-angle photonic and optoelectronic devices with strong light-matter interactions. This approach can be naturally extended to higher-dimensional systems, potentially revealing richer topological phenomena associated with flat bands, including nontrivial second Chern numbers and symmetry-protected higher-order topological states. Our findings on the dual topology of cascade flat bands might apply to more general 2D supermoiré lattices [71, 72] or hybrid structures that combine moiré and breathing geometries, where k_ϕ can act as a physical dimension. Such extensions suggest a deeper connection between flat-band physics and higher-dimensional analogs of LLs, holding potentials for investigating novel strongly correlated phenomena. Finally, the proposed breathing superlattice structure is versatile and not limited to photonic applications—it can also be applied to other physical systems, including magnons, optical lattices, and acoustic and elastic waves.

Methods

Numerical simulations

The band structures of the photonic crystal slabs were calculated by using the GME method implemented with the `legume` package [61]. PBC in the xy -plane were adopted, and the unit cell size in the y direction was set to $a_y = a_0/200$ to increase the computational efficiency. For the TM polarization, coupled odd guided modes with `gmode_inds=1,3,...,9` were utilized, and the convergence was ensured by including up to `gmax=60` guided modes.

The exact 1D optical simulations with both PBC and OBC were conducted using finite differences of the Maxwell operator, defined by $\Theta = -\frac{d}{dx} \left(\frac{1}{\varepsilon(x)} \frac{d}{dx} \right)$. The differential steps were adjusted according to the breathing strength δ to achieve fast convergence. For PBC, the Bloch momentum was implemented with twisted boundary conditions at the unit cell boundaries (see Supplementary S4 B for technique details). In OBC calculations, 10 unit cells were considered.

The dielectric structure was modeled as a periodic function $\varepsilon(x+a) = \varepsilon(x)$ containing N rectangular functions per unit cell (see Supplementary S4 A for construction of $\varepsilon(x)$), where $a = Na_0$ is the lattice constant. Inversion symmetry was enforced by setting $\varepsilon(x+a/2) = \varepsilon(x-a/2)$. The parameter $k_\phi \in [0, 2\pi)$ was used to shift the structure via $\varepsilon'(x) = \varepsilon(x+k_\phi a/2\pi)$, where the inversion symmetry is preserved only at $k_\phi = 0$ and $k_\phi = \pi$. The eigenvectors of the Θ operator were labeled as $|u_{nk}(k_\phi)\rangle = \sum_{x,k} u_{nk,x}(k_\phi)|x,k\rangle$ for PBC and as $|u_n(k_\phi)\rangle = \sum_x u_{n,x}(k_\phi)|x\rangle$ for OBC, where x denotes discrete sites within the unit cell (for PBC) or the entire system (for OBC).

Topological invariants of flat bands were computed via real-space simulations of the Θ operator with PBC cases. Bands are characterized by a \mathbb{Z}_2 Zak phase, depending on the shift parameter δ , with $k_\phi = 0$ for $\delta < 0$ and $k_\phi = \pi$ for $\delta > 0$. The Zak phase, corresponding to the Wannier center \bar{x}_n of the n th band, is defined as $\Phi_{\text{zak}}(k_\phi) = \int_{k \in \text{BZ}} dk \mathcal{A}_{nk}(k_\phi)$, where $\mathcal{A}_{nk}(k_\phi) = \langle u_{nk}(k_\phi) | \hat{x} | u_{nk}(k_\phi) \rangle$ and $\hat{x} = i\partial_k$. The Chern number is calculated by $C_n = \frac{1}{2\pi} \int_{\text{BZ}} dk \int_0^{2\pi} dk_\phi F_n$, where Berry curvature $F_n = \partial_k \mathcal{A}'_{nk} - \partial_{k_\phi} \mathcal{A}_{nk}$ and $\mathcal{A}'_{nk} = \langle u_{nk}(k_\phi) | i\partial_{k_\phi} | u_{nk}(k_\phi) \rangle$.

The high Q property of flat bands is demonstrated through RCWA calculation with S⁴ package [73], where the number of plane wave basis is set to be 108 for fast convergence. The geometric parameters are used as $a_0 = 190 \text{ nm}$, $\kappa = 0.6$, $\delta = 0.1$ and $h = 0.86a_0$.

Effective model

The plane wave expansion (PWE) method was utilized to develop an effective model accounting for the momentum-independent interband scattering. For the 1D breathing superlattice, the model is obtained by expanding Eq. (6) into a series of δ functions:

$$\tilde{\varepsilon}(g) = c\delta_{g,0} + \sum_{t \in \mathbb{Z}} \sum_{s=0}^{N-1} d_{t,s} \delta_{g,(tN+s)g_0}, \quad (9)$$

where $d_{t,u}$ depends on δ . Eq. (9) is equivalent to Eq. (6), and $d_{t,u}$ can be regarded as the scattering strength directly. Inserting Eq. (9) into Eq. (5) yields,

$$\hat{\Theta}(q) = \sum_i c(q+g_i)^2 \hat{b}_i^\dagger \hat{b}_i + \sum_{t,s} d_{t,u} h_q(g_i, g_i + (tN+s)g_0) \hat{b}_i^\dagger \hat{b}_{i+tN+s}. \quad (10)$$

By only considering the scatterings among the i th, $i \pm N$ th, and $i \pm (N \pm 1)$ th bands. Then the effective minimal model is given by:

$$\hat{\Theta}(q) = \sum_{i=0} c(q+g_i)^2 \hat{b}_i^\dagger \hat{b}_i + \sum_{s=-1,0,1} w_s(q) \hat{b}_i^\dagger \hat{b}_{i \pm (N+s)}, \quad (11)$$

where the parameters $c = 0.28$, $d_{1,0} = 0.176$, and $d_{0,N-1} = d_{1,1} = 0.014$ were fitted using direct diagonalization at $\delta = 0.07$. This effective model is formally analogous

to the CM for $w_s(q) \propto h_q(g_i, g_j)$, which indicate $w_s(q)$ is almost independent from q ($q \in (0, q_0] \ll g_i$).

Construction of 2D breathing lattices

For the partial flat bands lattice, the construction is the same as 1D cases, where the hole radius is set to be $r = 0.365(1 \mp \delta)a_0$.

For the 2D triangular superlattice, the lattice vectors are defined as $A_1 = N(2a_2 - a_1)$ and $A_2 = N(a_1 + a_2)$, where $a_1 = a_0[\sqrt{3}, 1]^T/2$, $a_2 = a_0[0, 1]^T$, and $N = 8$. In Fig. 6(b), $a = |A_i|$ is the lattice constant. The shift parameter δ divides the unit cell into four regions: $S_{++} : (m < 1/2, n < 1/2)$, $S_{+-} : (m \geq 1/2, n < 1/2)$, $S_{-+} : (m < 1/2, n \geq 1/2)$, and $S_{--} : (m \geq 1/2, n \geq 1/2)$, where (m, n) are the fractional coordinates of the lattice sites with respect to A_1 and A_2 . For the $S_{\pm\pm}$ regions, the lattice sites are generated as $p = i(1 \pm \delta)a_1 + j(1 \pm \delta)a_2$, where $i, j \in \mathbb{Z}$. The radius of the hole is specified as $0.365(1 + \delta)a_0$ in the S_{++} region and $0.365(1 - \delta)a_0$ in other regions.

Sample fabrication

The TiO_2 photonic crystal slabs were fabricated using the standard electron beam lithography (EBL) and atomic layer deposition (ALD) techniques followed by the inductively coupled plasma (ICP) etch process. The quartz substrate was first cleaned in the ultrasound bath with acetone and absolute ethyl alcohol for 10 minutes. Then, a 20 nm layer indium tin oxide (ITO) was deposited on the substrate by using magnetron sputtering method. After that, a PMMA film was spin-coated onto the ITO layer, and baked at 180°C for 2 min. Subsequently, the superlattice pattern was transferred to the PMMA resist by the EBL technique. TiO_2 was then deposited using ALD at 90°C with TiCl_4 and H_2O as the precursors and N_2 as the carrier gas. After that, the residual TiO_2 film coated on the top surface of PMMA was removed by the ICP etch in a mixture of Ar and SF_6 reactive gas. Finally, the remaining resist was removed and only the metagratings were left.

Optical spectroscopy characterization

The frequency-resolved momentum-space transmission spectra were measured by a commercial angle-resolved spectroscopy equipment ARMS based on the back focal plane imaging technique, which allowed probing the angular distribution of the sample's transmission by imaging the back focal plane of the collecting objective. The source is a tungsten lamp and the incident light was focused on to the sample by an objective (20 magnitude, $\text{NA} = 0.4$). A wire grid polarizer was used for implementing the polarization configuration. The transmitted light from the sample was sent to the slit of the CCD imaging spectrometer (Princeton Instruments HRS-300SS) with a grating (600 lines/mm) through a series of convex lens.

The experiment measurements were subsequently post-processed under the phase matching condition $p = \frac{2\pi}{\lambda} \sin(\phi)$ where λ is the wavelength and $-20^\circ \leq \phi \leq 20^\circ$ is incident angle. The Bloch momentum p was calculated by incorporating band folding, where $k = p + \frac{2\pi n}{a}$ with $a = Na_0$ is the lattice constant and n labels the reciprocal

lattices. The experimental data were discretely sampled on a two-dimensional grid, enabling a transformation from angle-dependent measurements to Brillouin zone.

References

- [1] Esaki, L., Tsu, R.: Superlattice and negative differential conductivity in semiconductors. *IBM J. Res. Develop.* **14**(1), 61–65 (1970) <https://doi.org/10.1147/rd.141.0061>
- [2] Yablonovitch, E.: Inhibited spontaneous emission in solid-state physics and electronics. *Phys. Rev. Lett.* **58**, 2059–2062 (1987)
- [3] John, S.: Strong localization of photons in certain disordered dielectric superlattices. *Phys. Rev. Lett.* **58**, 2486–2489 (1987)
- [4] Kushwaha, M.S., Halevi, P., Dobrzynski, L., Djafari-Rouhani, B.: Acoustic band structure of periodic elastic composites. *Phys. Rev. Lett.* **71**, 2022–2025 (1993)
- [5] Liu, Z., Zhang, X., Mao, Y., Zhu, Y.Y., Yang, Z., Chan, C.T., Sheng, P.: Locally resonant sonic materials. *Science* **289**(5485), 1734–1736 (2000)
- [6] Joannopoulos, J.D., Johnson, S.G., Winn, J.N., Meade, R.D.: *Photonic Crystals: Molding the Flow of Light*, 2nd edn. Princeton University Press, Princeton, NJ (2011). <https://books.google.com/books?id=QrTNSlcjlZEC>
- [7] Forn-Díaz, P., Lamata, L., Rico, E., Kono, J., Solano, E.: Ultrastrong coupling regimes of light-matter interaction. *Rev. Mod. Phys.* **91**, 025005 (2019)
- [8] González-Tudela, A., Reiserer, A., García-Ripoll, J.J., García-Vidal, F.J.: Light-matter interactions in quantum nanophotonic devices. *Nat. Rev. Phys.* **6**(3), 166–179 (2024)
- [9] Markos, C., Travers, J.C., Abdolvand, A., Eggleton, B.J., Bang, O.: Hybrid photonic-crystal fiber. *Rev. Mod. Phys.* **89**, 045003 (2017)
- [10] Roberts, N., Baardink, G., Nunn, J., Mosley, P.J., Souslov, A.: Topological supermodes in photonic crystal fiber. *Sci. Adv.* **8**(51), 3522 (2022)
- [11] Chen, W.T., Zhu, A.Y., Capasso, F.: Flat optics with dispersion-engineered metasurfaces. *Nat. Rev. Mater.* **5**(8), 604–620 (2020)
- [12] Silva, A., Monticone, F., Castaldi, G., Galdi, V., Alù, A., Engheta, N.: Performing mathematical operations with metamaterials. *Science* **343**(6167), 160–163 (2014)
- [13] Guo, C., Xiao, M., Minkov, M., Shi, Y., Fan, S.: Photonic crystal slab laplace operator for image differentiation. *Optica* **5**(3), 251–256 (2018)
- [14] Tang, L., Song, D., Xia, S., Xia, S., Ma, J., Yan, W., Hu, Y., Xu, J., Leykam,

- D., Chen, Z.: Photonic flat-band lattices and unconventional light localization. *Nanophotonics* **9**(5), 1161–1176 (2020)
- [15] Leykam, D., Flach, S.: Perspective: Photonic flatbands. *APL Photon.* **3**(7), 070901 (2018)
 - [16] Baboux, F., Ge, L., Jacqmin, T., Biondi, M., Galopin, E., al: Bosonic condensation and disorder-induced localization in a flat band. *Phys. Rev. Lett.* **116**, 066402 (2016)
 - [17] Xu, Z., Kong, X., Chang, J., Sievenpiper, D.F., Cui, T.J.: Topological flat bands in self-complementary plasmonic metasurfaces. *Phys. Rev. Lett.* **129**, 253001 (2022)
 - [18] Hoang, T.X., Leykam, D., Kivshar, Y.: Photonic flatband resonances in multiple light scattering. *Phys. Rev. Lett.* **132**, 043803 (2024)
 - [19] Li, J., White, T.P., O’Faolain, L., Gomez-Iglesias, A., Krauss, T.F.: Systematic design of flat band slow light in photonic crystal waveguides. *Opt. Express* **16**(9), 6227–6232 (2008)
 - [20] Amelio, I., Goldman, N.: Lasing in non-hermitian flat bands: Quantum geometry, coherence, and the fate of kardar-parisi-zhang physics. *Phys. Rev. Lett.* **132**, 186902 (2024)
 - [21] Zhou, Y., Guo, Z., Zhou, W., Li, S., Liu, Z., Zhao, X., Wu, X.: High-q guided mode resonance sensors based on shallow sub-wavelength grating structures. *Nanotechnology* **31**(32), 325501 (2020)
 - [22] Overvig, A.C., Cotrufo, M., Markowitz, M., Zhou, Y., Hao, B., Stensvad, K., Schardt, C., Alù, A.: Zone-folded quasi-bound state metasurfaces with customized, symmetry-protected energy-momentum relations. *ACS Photon.* **10**(6), 1832–1840 (2023)
 - [23] Yang, Y., Roques-Carmes, C., Kooi, S.E., Tang, H., Justin, B., al: Photonic flatband resonances for free-electron radiation. *Nature* **613**(7942), 42–47 (2023)
 - [24] Endo, S., Oka, T., Aoki, H.: Tight-binding photonic bands in metallophotonic waveguide networks and flat bands in kagome lattices. *Phys. Rev. B* **81**, 113104 (2010)
 - [25] Kollár, A.J., Fitzpatrick, M., Sarnak, P., Houck, A.A.: Line-graph lattices: Euclidean and non-euclidean flat bands, and implementations in circuit quantum electrodynamics. *Commun. Math. Phys.* **376**(3), 1909–1956 (2020)
 - [26] Ma, J., Rhim, J.-W., Tang, L., Xia, S., Wang, H., Zheng, X., Xia, S., Song, D., Hu, Y., Li, Y., Yang, B.-J., Leykam, D., Chen, Z.: Direct observation of flatband loop states arising from nontrivial real-space topology. *Phys. Rev. Lett.* **124**, 183901 (2020)

- (2020)
- [27] Scheer, M.G., Lian, B.: Twistronics of kekulé graphene: Honeycomb and kagome flat bands. *Phys. Rev. Lett.* **131**, 266501 (2023)
 - [28] Neves, P.M., Wakefield, J.P., Fang, S., Nguyen, H., Ye, L., Checkelsky, J.G.: Crystal net catalog of model flat band materials. *npj Comput. Mater.* **10**(1), 39 (2024)
 - [29] Danieli, C., Andreanov, A., Leykam, D., Flach, S.: Flat band fine-tuning and its photonic applications (2024) [arXiv:2403.17578](https://arxiv.org/abs/2403.17578) [physics.optics]
 - [30] Vicencio, R.A., Cantillano, C., Morales-Inostroza, L., Real, B., Mejía-Cortés, C., Weimann, S., Szameit, A., Molina, M.I.: Observation of localized states in lieb photonic lattices. *Phys. Rev. Lett.* **114**, 245503 (2015)
 - [31] Mukherjee, S., Spracklen, A., Choudhury, D., Goldman, N., Öhberg, P., Andersson, E., Thomson, R.R.: Observation of a localized flat-band state in a photonic lieb lattice. *Phys. Rev. Lett.* **114**, 245504 (2015)
 - [32] Kajiwara, S., Urade, Y., Nakata, Y., Nakanishi, T., Kitano, M.: Observation of a nonradiative flat band for spoof surface plasmons in a metallic lieb lattice. *Phys. Rev. B* **93**, 075126 (2016)
 - [33] Wang, F., Ran, Y.: Nearly flat band with chern number $c = 2$ on the dice lattice. *Phys. Rev. B* **84**, 241103 (2011)
 - [34] Călugăru, D., Chew, A., Elcoro, L., Xu, Y., Regnault, N., Song, Z.-D., Bernevig, B.A.: General construction and topological classification of crystalline flat bands. *Nat. Phys.* **18**(2), 185–189 (2022)
 - [35] Huda, M.N., Kezilebieke, S., Liljeroth, P.: Designer flat bands in quasi-one-dimensional atomic lattices. *Phys. Rev. Res.* **2**(4), 043426 (2020)
 - [36] Pal, B., Saha, K.: Flat bands in fractal-like geometry. *Phys. Rev. B* **97**(19), 195101 (2018)
 - [37] Bistritzer, R., MacDonald, A.H.: Moire bands in twisted double-layer graphene. *Proc. Natl. Acad. Sci. USA* **108**(30), 12233–12237 (2011)
 - [38] Tarnopolsky, G., Kruchkov, A.J., Vishwanath, A.: Origin of magic angles in twisted bilayer graphene. *Phys. Rev. Lett.* **122**(10), 106405 (2019)
 - [39] Angeli, M., MacDonald, A.H.: Γ valley transition metal dichalcogenide moiré bands. *Proc. Natl. Acad. Sci. USA* **118**(10), 2021826118 (2021)
 - [40] Zhang, D.-B., Seifert, G., Chang, K.: Strain-induced pseudomagnetic fields in twisted graphene nanoribbons. *Phys. Rev. Lett.* **112**, 096805 (2014)

- [41] Bi, Z., Yuan, N.F.Q., Fu, L.: Designing flat bands by strain. *Phys. Rev. B* **100**(3), 035448 (2019)
- [42] Wan, X., Sarkar, S., Lin, S.-Z., Sun, K.: Topological exact flat bands in two-dimensional materials under periodic strain. *Phys. Rev. Lett.* **130**, 216401 (2023)
- [43] Gao, Q., Dong, J., Ledwith, P., Parker, D., Khalaf, E.: Untwisting moiré physics: Almost ideal bands and fractional chern insulators in periodically strained monolayer graphene. *Phys. Rev. Lett.* **131**(9), 096401 (2023)
- [44] Ke, S., Li, Y.-M., Lou, W.-K., Chang, K.: Pure magnon valley currents in a patterned ferromagnetic thin film. *Phys. Rev. B* **107**, 104426 (2023)
- [45] Wei, B., Zhu, J.-J., Song, Y., Chang, K.: Strain-engineered magnon states in two-dimensional ferromagnetic monolayers. *Phys. Rev. Res.* **6**, 013210 (2024)
- [46] Wang, P., Zheng, Y., Chen, X., Huang, C., Kartashov, Y.V., Torner, L., Konotop, V.V., Ye, F.: Localization and delocalization of light in photonic moiré lattices. *Nature* **577**(7788), 42–46 (2020)
- [47] Mao, X.-R., Shao, Z.-K., Luan, H.-Y., Wang, S.-L., Ma, R.-M.: Magic-angle lasers in nanostructured moiré superlattice. *Nat. Nanotechnol.* **16**(10), 1099–1105 (2021)
- [48] Dong, K., Zhang, T., Li, J., Wang, Q., Yang, F., Rho, Y., Wang, D., Grigoropoulos, C.P., Wu, J., Yao, J.: Flat bands in magic-angle bilayer photonic crystals at small twists. *Phys. Rev. Lett.* **126**, 223601 (2021)
- [49] Tang, H.N., Du, F., Carr, S., DeVault, C., Mello, O., Mazur, E.: Modeling the optical properties of twisted bilayer photonic crystals. *Light Sci. Appl.* **10**(1), 157 (2021)
- [50] Oudich, M., Su, G., Deng, Y., Benalcazar, W., Huang, R., Gerard, N.J.R.K., Lu, M., Zhan, P., Jing, Y.: Photonic analog of bilayer graphene. *Phys. Rev. B* **103**, 214311 (2021)
- [51] Nguyen, D.X., Letartre, X., Drouard, E., Viktorovitch, P., Nguyen, H.C., Nguyen, H.S.: Magic configurations in moiré superlattice of bilayer photonic crystals: Almost-perfect flatbands and unconventional localization. *Phys. Rev. Res.* **4**, 032031 (2022)
- [52] Wang, H., Ma, S., Zhang, S., Lei, D.: Intrinsic superflat bands in general twisted bilayer systems. *Light Sci. Appl.* **11**(1), 159 (2022)
- [53] Tang, H., Lou, B., Du, F., Zhang, M., Ni, X., Xu, W., Jin, R., Fan, S., Mazur, E.: Experimental probe of twist angle-dependent band structure of on-chip optical bilayer photonic crystal. *Sci. Adv.* **9**(28), 8498 (2023)

- [54] Qin, H., Chen, S., Zhang, W., Zhang, H., Pan, R., Li, J., Shi, L., Zi, J., Zhang, X.: Optical moiré bound states in the continuum. *Nat. Comm.* **15**(1), 9080 (2024)
- [55] Graf, A., Piéchon, F.: Designing flat-band tight-binding models with tunable multifold band touching points. *Phys. Rev. B* **104**, 195128 (2021)
- [56] Bae, J.-H., Sedrakyan, T., Maiti, S.: Isolated flat bands in 2D lattices based on a novel path-exchange symmetry. *SciPost Phys.* **15**, 139 (2023)
- [57] Harper, P.G.: Single band motion of conduction electrons in a uniform magnetic field. *Proc. Phys. Soc. Sect. A* **68**(10), 874 (1955)
- [58] Wang, X.-H., Wang, J.J., Wang, J., Liu, J.-F.: Flat band assisted topological charge pump in the dice lattice. *Phys. Rev. B* **103**, 195442 (2021)
- [59] Su, W.P., Schrieffer, J.R., Heeger, A.J.: Solitons in polyacetylene. *Phys. Rev. Lett.* **42**, 1698–1701 (1979)
- [60] Miao, W., Li, C., Han, X., Pan, D., Dai, X.: Truncated atomic plane wave method for subband structure calculations of moiré systems. *Phys. Rev. B* **107**, 125112 (2023)
- [61] Minkov, M., Williamson, I.A.D., Andreani, L.C., Gerace, D., Lou, B., Song, A.Y., Hughes, T.W., Fan, S.: Inverse design of photonic crystals through automatic differentiation. *ACS Photon.* **7**(7), 1729–1741 (2020)
- [62] Avron, J.E., Osadchy, D., Seiler, R.: A topological look at the quantum hall effect. *Physics Today* **56**(8), 38–42 (2003)
- [63] Qi, X.-L., Hughes, T.L., Zhang, S.-C.: Topological field theory of time-reversal invariant insulators. *Phys. Rev. B* **78**, 195424 (2008)
- [64] Nasidi, I., Hao, R., Jin, S., Li, E.: Flat bands and quasi-bound states in the continuum in a photonic moiré lattice. *J. Opt. Soc. Am. B* **40**(2), 260–265 (2023)
- [65] Ouyang, Y.-H., Luan, H.-Y., Zhao, Z.-W., Mao, W.-Z., Ma, R.-M.: Singular dielectric nanolaser with atomic-scale field localization. *Nature* **632**(8024), 287–293 (2024)
- [66] Sun, K., Wei, H., Chen, W., Chen, Y., Cai, Y., Qiu, C.-W., Han, Z.: Infinite-q guided modes radiate in the continuum. *Phys. Rev. B* **107**, 115415 (2023)
- [67] Conteduca, D., Reardon, C., Scullion, M.G., Dell’Olio, F., Armenise, M.N., Krauss, T.F., Ciminelli, C.: Ultra-high q/v hybrid cavity for strong light-matter interaction. *APL Photon.* **2**(8), 086101 (2017)
- [68] Luan, H.-Y., Ouyang, Y.-H., Zhao, Z.-W., Mao, W.-Z., Ma, R.-M.: Reconfigurable

- moiré nanolaser arrays with phase synchronization. *Nature* **624**(7991), 282–288 (2023)
- [69] Danieli, C., Andreanov, A., Mithun, T., Flach, S.: Nonlinear caging in all-bands-flat lattices. *Phys. Rev. B* **104**, 085131 (2021)
 - [70] Choi, M., Munley, C., Frösch, J.E., Chen, R., Majumdar, A.: Nonlocal, flat-band meta-optics for monolithic, high-efficiency, compact photodetectors. *Nano Lett.* **24**(10), 3150–3156 (2024). doi: 10.1021/acs.nanolett.3c05139
 - [71] Devakul, T., Ledwith, P.J., Xia, L.-Q., Uri, A., Barrera, S.C., Jarillo-Herrero, P., Fu, L.: Magic-angle helical trilayer graphene. *Sci. Adv.* **9**(36), 6063 (2023)
 - [72] Al Ezzi, M.M., Hu, J., Ariando, A., Guinea, F., Adam, S.: Topological flat bands in graphene super-moiré lattices. *Phys. Rev. Lett.* **132**(12), 126401 (2024)
 - [73] Liu, V., Fan, S.: S^4 : A free electromagnetic solver for layered periodic structures. *Comput. Phys. Commun.* **183**(10), 2233–2244 (2012)

Figures

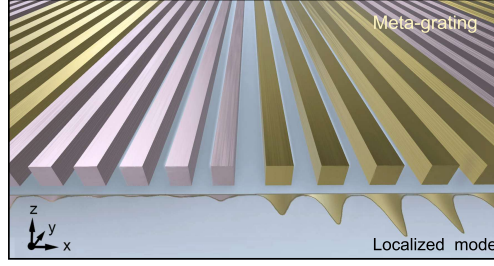


Fig. 1 Schematic of the breathing superlattice. Here, the eigenfield of the flat bands is localized in the shrunken sublattice.

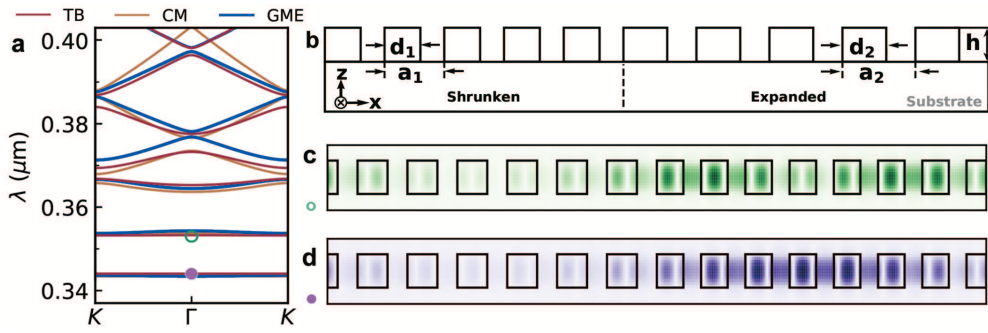


Fig. 2 Analytical and photonic flat bands. (a) Band structures of a 1D breathing superlattice with $N = 14$ for TM polarization. The fitting TB parameters are $\mu_i = 730$, $t_0 = 60$ THz, $\delta_T = 0.25$. The fitting CM parameters are $\mu = 850$, $m^* = 1.7$, and $(w_1, w_2, w_3, w_4) = (18, 2.88, -4.32, 0.72)$ THz. (b) Cross-sectional view of the proposed PhCS. (c, d) Electric field distributions at the Γ point for higher and lower flat bands.

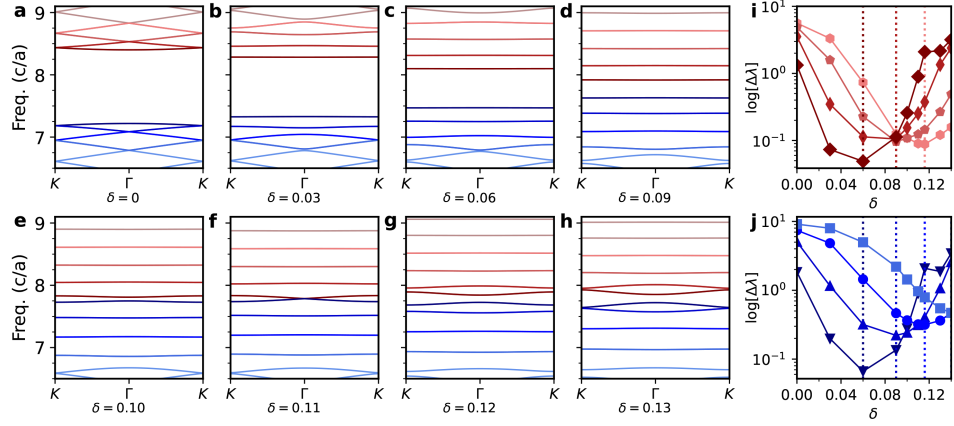


Fig. 3 Photonic flat bands engineering. (a-h) Evolution of flat bands for the TM-polarization of PhCSs with $N = 14$ and δ varying from 0 to 0.14. Here, the lattice constant is $a = 2.66 \mu m$. (i,j) Dependence of the bandwidth ($\Delta\lambda$) of conduction (red) /valence (blue) bands on δ .

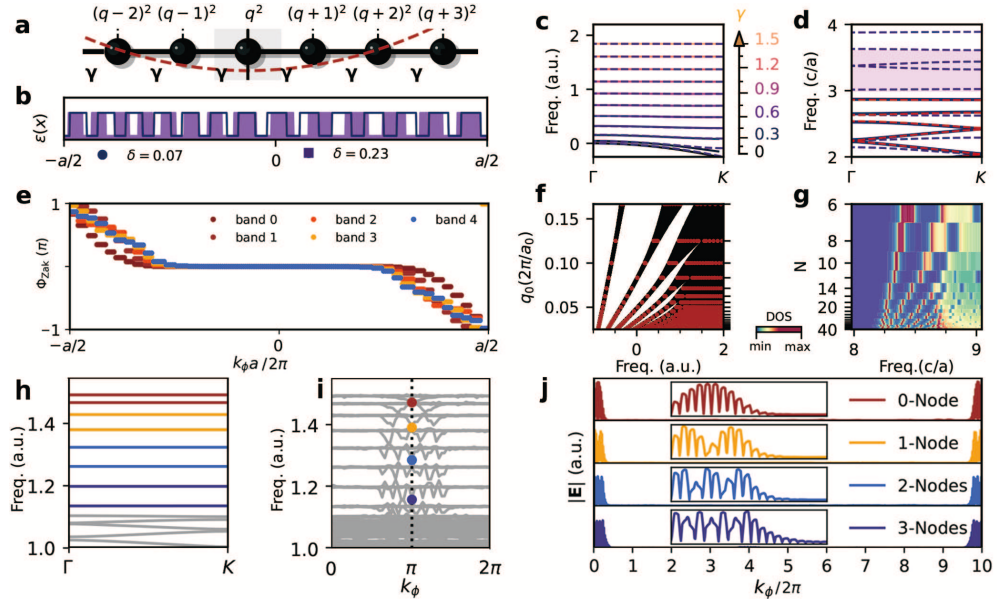


Fig. 4 Physical origins of flat bands. (a) The CM lattice model in momentum space. (b) Permittivity distribution for $\delta = 0.07$ (blue) and 0.23 (purple). (c) Analytical (purple) and numerical (dashed) evolution of the zeroth flat band with γ . (d) Band structure calculated with the $\hat{\Theta}$ operator for $\delta = 0.23$, $N = 14$ (dashed purple), numerical diagonalization for $\delta = 0.17$ (solid blue), and the effective model (dashed red) (See Method). (e) ϕ_{zak} for the first 4 bands in (h). (f) Dependence of the energy spectrum on q_0 , where red points correspond to $q_0 = 2\pi/Na_0$ with even N . (g) Dependence of DOS on frequency and N for $\delta = 0.03$. (h) Band structure calculated from $\hat{\Theta}$ for $N = 40$, $\delta = 0.15$. (i) Energy spectrum of the finite lattice with respect to k_ϕ . (j) Topological edge states at frequencies marked in (i). Inset: Field patterns of the edge states.

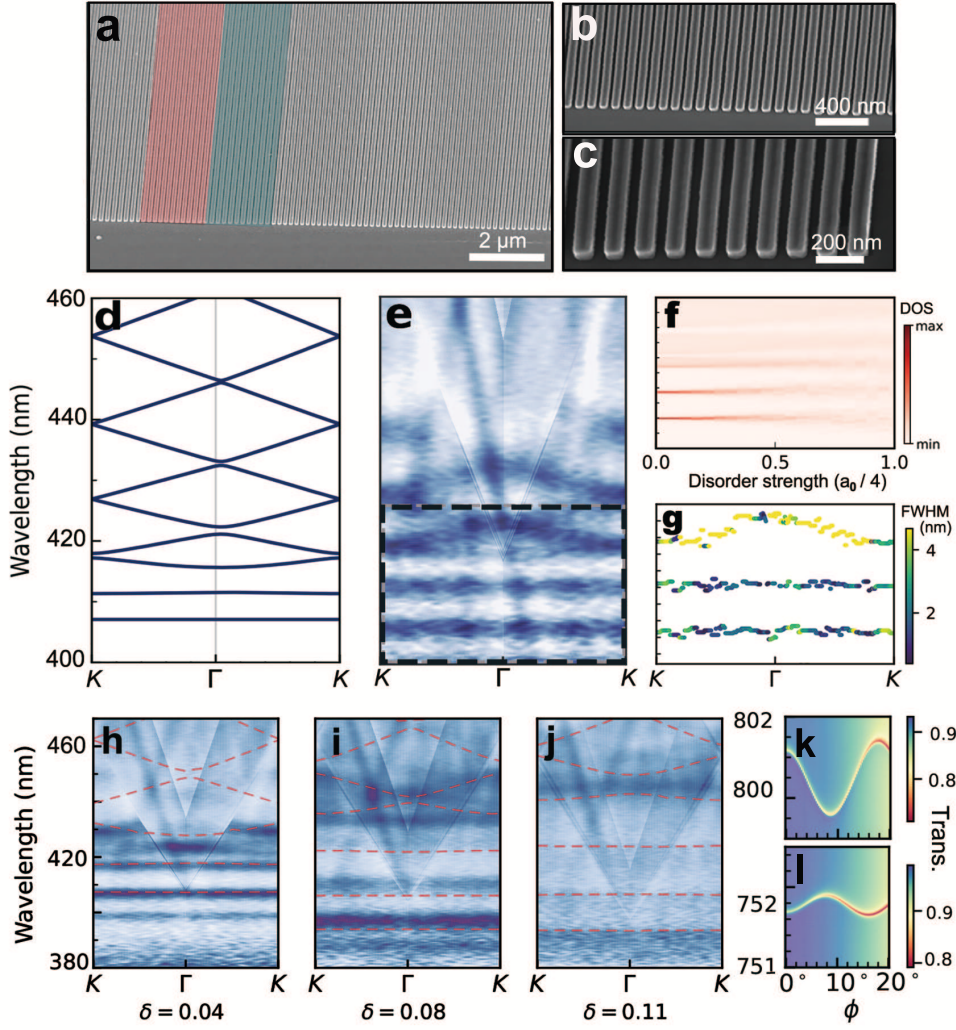


Fig. 5 Experimental results. (a-c) SEM images of fabricated TiO₂ PhCS. Simulated (d) and measured (e) photonic bands for the TM-polarization with the structure parameters $N = 24$, $\delta = 0.018$, $\kappa = 0.6$, $a_0 = 202.95$, $h = 144$ nm and $h_s = 20$ nm. (f) Evolution of DOS of flat bands on intra-cell disorder for 100 samples. (g) FWHM extracted from the experimentally measured spectrum (see Supplementary S10), which indicating the leakage of the eigen-modes. (f) and (g) share the same energy window marked in (e). (h-j) Measured and calculated bands (dashed) for the TM-polarization of PhCSs with $N = 14$. The structure parameters are tabled in (see Supplementary Tab. S2) and the dashed line are GME band structures. (k-l) RCWA calculated high Q flat bands for 0th and 1st LLs of a free standing sample.

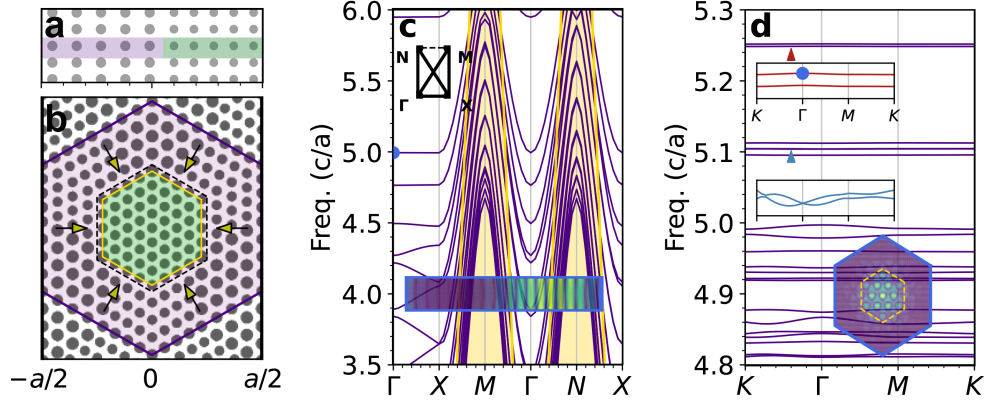


Fig. 6 2D generation of photonic flat bands. (a) Superlattice along only the x -directions with thickness $h = 0.6a_0$. (b) Triangular superlattice on both directions with thickness $h = 0.6a_0$. (c) TM-polarized photonic band structures with partial flat bands, the shaded region represents modes below the light-line. (d) Omnidirectional flat bands for a PhCS with superlattice shown in (b). Insets in (c,d) are the corresponding BZs and field distributions of $|\mathbf{H}|$ for flat bands at the Γ point.

Acknowledgments

This work is supported by Chinese Academy of Sciences (CAS, No. XDB28000000, No. QYZDJ-SSWSYS001, No. XDPB22 and XDB0460000), National Natural Science Foundation of China (No. 61875225 and No. 12374282) and Innovation Program for Quantum Science and Technology (Grant No. 2024ZD0300104)

Author contribution

M.S., Y.Z conceived the project idea and K.C. supervised the project. M.S. develop the theoretical back ground and perform the simulations. M.S., Y.Z and K.C. wrote the manuscript. Y.Z provide support on the AMRS test environment, J.H and L.S performed the fabrication of sample and provide support on SEM image. All author contribute to the data analysis and proofread the manuscript.

Competing interests

The authors declare no competing interests.

Additional information

Supplementary information. We provide a comprehensive overview of both the theoretical underpinnings and the experimental procedures that support our main findings. In S1, we derive the continuum model that forms the cornerstone of our analysis and in S2, we establish its duality with the Harper-Hofstadter model. In S3, the geometric phases of the system, including the Zak phase and edge states, are discussed in detail, and in S4, we introduce the Θ -operator in one dimension, supplemented with both plane-wave expansion and real-space finite discretization approaches. In S5, we present the eigen-field distributions at key momentum points, while S6 offers a derivation of the rate at which an energy gap opens in our model. The system's robustness to intra-cell disorder is investigated in S7, and an analytic dispersion relation from the continuum model is formulated in S8. We address the renormalization of γ by scaling N in S9, and outline the protocols for experimental measurement and data post-processing in S10. Finally, in S11, we extend our concepts to demonstrate how cascading two-dimensional flat bands can emerge from the framework introduced here. These sections collectively ensure the rigor of our conclusions and offer detailed insights for further exploration.